Hindawi
Advances in Civil Engineering
Volume 2024, Article ID 7126022, 18 pages
https://doi.org/10.1155/2024/7126022

Research Article

Investigation on Dynamic Stability of Cement-Stabilized Expansive Soil Subgrades Subjected to Repeated Heavy-Haul Train Loads

Yonghui Shang,[1,2] **Linrong Xu**,[2,3] **Xiaofei Hao**,[4] **Qichuan Zhu**,[5] **and Donghong Li**[5]

[1]*Institute of Architecture and Engineering, Huanghuai University, Zhumadian 463000, Henan, China*
[2]*School of Civil Engineering, Central South University, Changsha 410075, Hunan, China*
[3]*National Engineering Research Center for High-Speed Railway Construction Technology, Central South University, Changsha 410075, Hunan, China*
[4]*School of Chemical Engineering, Zhengzhou University, Zhengzhou 450001, China*
[5]*Henan Zhonglian Tongli Material Co. Ltd., Zhengzhou 450001, China*

Correspondence should be addressed to Yonghui Shang; 1400391317@qq.com

Received 17 January 2024; Revised 15 April 2024; Accepted 18 April 2024; Published 30 April 2024

Academic Editor: Fan Gu

The dynamic characteristics of the filler are intricately linked to the stability of the subgrade. In this investigation, relying on Haoji (Haolebaoji-Ji'an, China) heavy-haul railway engineering, cyclic triaxial tests were executed to scrutinize the dynamic attributes exhibited by the 3%–5% cement-stabilized expansive soil (CSES) across a series of diverse cyclic stress, confining pressures, and frequencies. Concurrently, in situ vibration trials were undertaken to dissect the dynamic characteristics inherent to the CSES subgrade. The outcomes of cyclic triaxial tests indicate that the augmentation in both the dynamic shear strength and modulus of CSES by a factor of 2–3, coupled with an escalation of the critical dynamic stress threshold by five tosix times, is attributed to the heightened internal structural density within the CSES compared to virgin expansive soil. In identical settings, it is noteworthy that the mean critical dynamic stress threshold observed for CSES surpasses that of Group A filling by a factor of 1.5–1.7. Furthermore, the maximum critical dynamic stress exhibited by CSES achieves a 1.2-fold superiority over its lime-stabilized expansive soil (LSES). The outcomes gleaned from the in situ vibration tests elucidate that, when subjected to the passage of a high-velocity train traveling at 120 km/hr, bearing the load of 25–30 tons per axle, the subgrade surface exhibits dynamic stress ranging from 98.57 to 116.07 kPa. Meanwhile, the dynamic stress undergoes a notable escalation due to rainfall infiltration, intensifying by a factor of 1.02–1.28 times its original magnitude. The influence depth of dynamic stress extends 1.4–1.6 times beyond the designed subgrade bed thickness of 2.5 m. Notably, the critical dynamic stress of the filler surpasses the dynamic stress at the same position, underscoreing the capacity of 3%–5% CSES filling for heavy-haul railways to ensure long-term dynamic stability.

1. Introduction

Utilizing expansive soils as fill material for embankments presents common engineering challenges such as volume changes causing instability, concerns regarding slope stability, susceptibility to cracking in arid conditions, risks of uneven settlement, potential erosion issues, and a higher probability of construction delays necessitating specialized mitigation strategies. The utilization of cement for enhancing the properties of substandard soil has been extensively adopted [1–4]. Cement-treated expansive soil emerges as a favorable option for serving as a substitute filler material for railway embankments in the absence of premium-grade fillers. The heavy-haul railway has gained prominence as the primary focus of freight railway development in numerous countries due to its substantial cargo capacity. In contrast to conventional and high-speed railway, the heavy-haul railway subgrade exhibits a notably heightened degree of dynamic response.

In light of the intricate dynamics inherent to the system under scrutiny, the analysis was initially performed with the classical theory of mechanics [5]. An elastic foundation beam

model was proposed by Daloglu et al. [6] for the analysis of track mechanics and subsequently validated by Fryba [7]. Based on the aforementioned investigations, the steady-state response of the elastic foundation beam under a constant velocity moving load was investigated by Krylov et al. [8]. In the contemporary landscape of railway dynamics, the intertwined vibrational interplay involving the train, track, and subgrade has been the focus of extensive inquiry. Remarkably, the scholarly endeavors of both Zhai et al. [9] and Chen and Bian [10] have culminated in a consensus: the contemplation of the interplay among the train, track, subgrade, and foundation is necessitated to acquire the dynamic exertions imparted by a moving train upon the tapestry of the track structure.

In tandem with the advancement of theoretical methodologies and computational capabilities, numerical simulation has emerged as an indispensable tool for delving into dynamic phenomena. In a three-dimensional (3D) numerical model, dynamic stress ranging from 74.60 to 119.37 kPa at the subgrade surface was identified under conditions involving a train speed of 120 km/hr and axle loads ranging from 25 to 40 tons [11]. Similarly, a corresponding dynamic stress range of 76.92–101.47 kPa was determined at the setting of a train speed of 120 km/hr and axle loads between 25 and 35 tons [12]. However, theoretical analyses and numerical simulations rely on numerous assumptions, demanding rigorous validation for their credibility.

In contrast, testing remains the most direct and dependable approach to investigating the dynamic characteristics of the subgrade. For instance, a full-scale subgrade model test was conducted by Leng et al. [13], and the results indicate that the dynamic stress experienced at the subgrade surface falls within the range of 64–90.1 kPa at the setting of train speeds of 80 km/hr and axle loads ranging from 25 to 30 tons. Nonetheless, model testing is not without its inherent limitations, given that reduced-scale model tests remain susceptible to substantial experimental errors stemming from scale effects, while full-scale model tests face formidable obstacles in accurately replicating the intricate dynamics of infinite domain foundation problems.

Because of the advancement of loading systems and testing technology, field testing has become instrumental in analyzing the dynamic characteristics of the subgrade. The dynamic characteristics of expansive soil cutting subgrade beds in high-speed railways were scrutinized via field vibration tests [14]. Simultaneously, the dynamic attributes of pile-slab composite foundations in transition sections of high-speed railways were examined in the study undertaken by Li et al. [15]. A in situ train test was conducted on the Shuohuang (Shenchi–Huanghua, China) heavy-haul railway by the China Academy of Railway Sciences, and the results yielded a dynamic stress range at the subgrade surface ranging from 110.1 to 123.0 kPa, given an axle load of 25–30 tons [16].

The strength of the subgrade decreases under prolonged and repetitive dynamic loading, leading to deformation that can ultimately affect the operational performance of the roadbed during its service life. Hence, it is of paramount importance to analyze the dynamic characteristics of the fill material. Among these characteristics, the dynamic elastic modulus and damping ratio emerge as two crucial parameters that define the apparent dynamic behavior of the soil. For instance, an empirical expression was formulated to determine the maximum shear modulus of normally consolidated clay [17]. A formula was introduced to estimate the maximum dynamic shear modulus of cohesive soil based on the consolidated undrained shear strength [18]. Additionally, it was determined that the dynamic modulus and damping ratio of Group A filling for high-speed railways increased with higher strain levels [19]. Interestingly, it was observed that the vibration frequency had minimal impact on the dynamic modulus of the filler at the setting of low dynamic stress amplitude.

Recognizing the critical role of settlement in ensuring the safety of railway operations, several scholars have conducted investigations into the cumulative deformation characteristics of fillers through cyclic triaxial tests. For example, a modified model was proposed to explore the cumulative deformation of sand, taking into account pore pressure and loading history [20]. The investigation [21] delves into the influence of various factors (confining pressure, dynamic stress, and drainage conditions) on the cumulative deformation of silt. The feasibility of LSES as the filler of high-speed railways was evaluated by the critical dynamic stress method [22]). It is generally accepted that the dynamic stability of the subgrade can be in a stable state when the actual dynamic stress within the subgrade is lower than its critical dynamic stress. Currently, there is a relative scarcity of research on the dynamic characteristics of CSES subjected to the dynamic loads imposed by heavy-haul railway trains.

In summary, significant progress has been achieved in the investigation of the dynamic characteristics of the subgrades under train-induced dynamic loads. However, the majority of studies have concentrated on load conditions associated with general-speed railways or high-speed railways, with relatively limited research dedicated to the dynamic attributes of heavy-haul railway subgrades. In this study, relying on Haoji heavy-haul railway engineering, cyclic triaxial tests were executed to scrutinize the dynamic attributes exhibited by the 3%–5% CSES across a series of diverse cyclic stress, confining pressures, and frequencies. Concurrently, in situ vibration trials were undertaken to dissect the dynamic characteristics inherent to the CSES subgrade. The findings of this investigation can offer valuable theoretical support for the implementation of subgrade projects in expansive soil regions within the context of heavy-haul railway infrastructure.

2. Methodology

2.1. Cyclic Triaxial Test. Soil samples were sourced from the vicinity of Dashanzhai near Dengzhou City, China (see Figure 1(a)). In the tests, P.O42.5 type Portland cement was employed to improve the expansive soil, with the cement content ranging from 3% to 5%. The optimal moisture content for CSESs with cement contents of 3%, 4%, and 5% are determined as 11.4%, 12.1%, and 13.5%, respectively. The specimens were cured at a temperature of around 20−30°C and relative humidity maintained at approximately 95% for a

(a) (b)

Figure 1: Cyclic triaxial test. (a) Soil sample. (b) DST-1 triaxial test system.

Table 1: The physical and mechanical of virgin expansive soil and CSES.

Category	Parameter	Natural soil sample	Cement content		
			3%	4%	5%
Particle size distributions (%)	>0.075 mm	5.4	20.5	21.1	23
	0.075–0.005 mm	50.3	52.2	55.8	55.0
	<0.005 mm	44.3	27.3	23.1	22.0
Swelling–shrinking characteristic	Free swelling ratio (%)	66	32	28	23
	Swelling ratio with loading (25 kPa)	6.8	0.1	0.06	<0
	Swelling ratio with loading (50 kPa)	6.7	<0	<0	<0
	Expansion force (kPa)	129	14	10	1
	Shrinkage coefficient	0.91	0.73	0.62	0.52
	Plastic limit (%)	10.2	10.2	11.9	11.2
Strength index	Cohesive force (kPa)	45	183	201	291
	Friction angle (°)	21.4	24.6	33.2	35.5
	Unconfined compressive strength test (7 days) (kPa)	44	866	1,018	1,170
Water-related stability coefficient	Degree of compaction (0.90)	0.18	0.81	0.84	0.83
	Degree of compaction (0.95)	0.25	0.85	0.88	0.89

curing period of 7–28 days to achieve optimal strength and stabilization effects. The physical and mechanical parameters of virgin expansive soil and CSES are shown in Table 1. As indicated in Table 1, the incorporation of cement into the expansive soil led to a decrease in fine particle content, an increase in coarse particle content, a significant enhancement in strength and water stability, and a notable improvement in expansion and contraction properties.

A comparison of certain indices between cement and lime improvement is presented in Table 2. Apparently, there is a minimal difference in the reduction of soil expansion and contraction between cement and lime improvement. However, in terms of enhancing soil strength, cement improvement demonstrates superior performance, making it more favorable for enhancing the stability of the subgrade in heavy-haul railways as a filler.

In this test, the DTS-1 microcomputer interface electromagnetic vibration triaxial test system was employed (see Figure 1(b)). The soil sample used had a cylindrical shape with a diameter of 39.1 mm and a height of 80 mm. The sample was compacted to a degree of compaction of 95%, and it was cured for 28 days. According to Lv et al. [12], the confining pressure applied to the samples was set at 15, 30, and 60 kPa, aiming to replicate lateral pressure conditions within a 3-m range of the subgrade bed for heavy-haul railways. Taking into account the specific characteristics of train load applications, single-width vibration sine waves were employed. The loading stress amplitude was carefully regulated to fall within the range of 20–250 kPa. The soil sample failure criteria were established as follows: if the accumulated strain reached 15% or if variables smaller than 0.1 mm persisted continuously for a duration of 15 min on three separate occasions during the integrity test, the test would be promptly terminated. Loading schedules are presented in Table 3.

2.2. In Situ Vibration Test. The in situ vibration test was carried out on section DK948 + 275 of the Haoji heavy-haul railway. In this section, the upper surface layer (0.6 m) of the subgrade bed was comprised of Group A filling, the

Table 2: Comparison of some indexes of expansion soils improved with cement and lime.

Category	Natural soil sample	Ratio (3%)		Ratio (4%)		Ratio (5%)	
		Cement	Lime	Cement	Lime	Cement	Lime
Free swelling ratio (%)	66	32	27	28	24	23	21
Swelling ratio with loading (25 kPa)	6.8	0.1	<0	0.06	<0	<0	<0
Swelling ratio with loading (50 kPa)	6.7	<0	<0	<0	<0	<0	<0
Expansion force (kPa)	129	14	12	10	5	1	1
Unconfined compressive strength test (7 days) (kPa)	44	866	308	1,018	477	117	786

Table 3: Loading schedules.

Category	Dry density (g/cm^3)	Frequency (Hz)	Confining pressure (kPa)
Virgin expansive soil	1.67	1, 5	15, 30, 60
Expansive soil improved with 3% cement content	1.72	1, 5	15, 30, 60
Expansive soil improved with 5% cement content	1.72	1, 5	15, 30, 60

(a) (b)

Figure 2: In situ vibration test. (a) ZBS60. (b) Infiltration simulation.

lower layer (1.9 m) of the subgrade bed was filled with 5% CSES, and the embankment below the lower subgrade bed layer was filled with 3% CSES.

To simulate the dynamic loads, a large-scale vibration exciter (ZBS60 Frequency-Converting and Torque-Changing Vibration Exciter) in conjunction with a concrete counterweight was employed to replicate the dynamic effects associated with a heavy-haul train operating at a speed of 120 km/hr and featuring axle loads ranging from 25 to 30 tons (see Figure 2(a)). Subsequently, the results were compared with those obtained from a simulation of a passenger train traveling at speeds between 120 and 200 km/hr, equipped with 21-t axle loads. Referring to Yang et al. [22], it was confirmed that the contact area between the concrete counterweight and the subgrade surface was 1.5 m^2. The dynamic stress range of the subgrade surface of heavy-haul railway is 80–130 kPa [10, 12, 16]. In the test, the dynamic stress amplitude of the excitation loading curve (sinusoidal curve) covers 70–140 kPa by adjusting the frequency and eccentric moment of the exciter. Simultaneously, recognizing that the dynamic stress experienced in actual railway subgrades represents a flexible load, a 0.15 m ballast was strategically placed beneath the excitation platform to closely approximate the simulated dynamic stress to actual conditions.

Rainfall infiltration was simulated by introducing water into the cofferdam. The dimensions of the cofferdam were 3.5 m in length, 3.5 m in width, and 0.2 m in height (see Figure 2(b)). As there was no readily available water source near the test site, water was introduced into the cofferdam using a water tanker. Once the water level had risen to a height of 20 cm, the drop in water level height was monitored at 10-min intervals. To ensure complete water infiltration, this water injection process was repeated twice, and the excitation test was initiated following a 24-hr interval to allow for adequate infiltration [10].

Figure 3 illustrates a schematic of the sensor installation for the test section. In accordance with the characteristics of the vibration test and the sensor types documented in references [14–16, 22], the JMYJ-1503 dynamic pressure box and the CA-YD-117 accelerometer were chosen. Meanwhile, the 60-channel IMC acquisition system was used to collect test data.

3. Result Analysis and Discussion

3.1. Dynamic Shear Strength. Dynamic shear strength pertains to the dynamic stress amplitude that the soil specimen must endure through N repetitions of a specific dynamic load

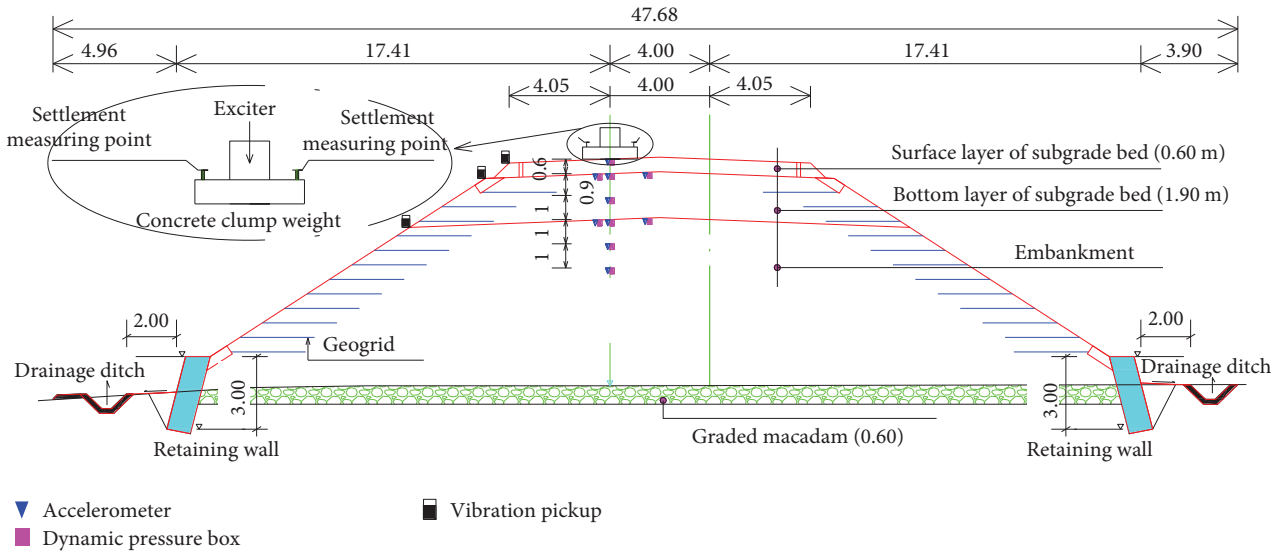

FIGURE 3: The schematic of the sensor installation for the test section (DK948 + 275).

to achieve a predetermined failure criterion. Figure 4 illustrates that the relationship curve between shear strength and failure vibration number τ_d–lg (N_f) for virgin expansive soil and expansive soils improved with 3% and 5% cement content ($\tau_d = \sigma_d/2$, τ_d is the dynamic shear stress on the 45° shear plane of the sample, σ_d is the axial dynamic stress, and N_f is the number of vibrations to reach the failure standard).

Figure 4 reveals that, in comparison to virgin expansive soil, the dynamic shear strengths of 3%–5% CSES exhibit a two to threefold increase. Dynamic shear strength has an evident reinforcing trend as confining pressure and consolidation ratio increase, indicating that the dynamic shear strengths of virgin expansive soil and CSES are mainly related to soil properties and initial stress state. In contrast to the impact of confining pressure, the influence of frequency on dynamic shear strength is relatively weaker. Additionally, the dynamic shear strengths of cement-stabilized soil exhibit a mild increasing trend of approximately 20%–25% with changes in frequency.

Given the applicability of the Mohr–Coulomb theory for analyzing soil dynamics [20], the shear strength curve for the same consolidation ratio was employed. It involved cutting off the dynamic shear stress τ_d corresponding to a failure vibration number under various confining pressures. Subsequently, σ_d was determined using the formula $\tau_d = \sigma_d/2$, as elaborated in Equations (1)–(3).

$$\sigma_{1d} = \sigma_1 + \sigma_d \quad (1)$$

$$\sigma_{3d} = \sigma_3 \quad (2)$$

$$\sigma_1 = K_c \sigma_3, \quad (3)$$

where σ_{1d} and σ_{3d} are the major and minor stresses of the soil sample when a dynamic failure occurs under the consolidation stress.

A Mohr circle of dynamic stress can be derived from σ_{1d} and σ_{3d} values. Subsequently, dynamic shear parameters, including cohesion c_d and friction angle φ_d under various test conditions, are determined from the dynamic shear strength envelope constructed using the three dynamic Mohr circles. The cohesive force c_d and friction angle φ_d were calculated for both virgin and improved expansive soil, with the latter including soil improved with 3% and 5% cement content, at a failure vibration cycle of 100 times, as demonstrated in Table 4.

Figure 5 illustrates that the dynamic shear parameter cohesion c_d exhibits a nearly linear increase with rising cement content. Conversely, the friction angle φ_d demonstrates an initial increase followed by a subsequent decrease as the cement content varies. Due to the solidification process with cement, the cohesion of the CSES will inevitably increase, while the friction angle tends to decrease when the cement content exceeds 3%. This phenomenon can be primarily attributed to the ion exchange and agglomeration effects of cement, leading to the bonding of most granular structures. Consequently, this process increases the presence of pores within the structure, thereby reducing the friction surface between soil particles and ultimately diminishing dynamic friction. As the frequency increases, it is observed that the cohesion c_d experiences an increase, while the friction angle φ_d undergoes a decrease. This trend can be attributed to the reduced time available for particle sliding and deformation within the sample under high-frequency vibrations, causing a decrease in interparticle friction. Additionally, the higher frequency vibrations result in more frequent particle interactions, which in turn contribute to an increase in cohesion.

3.2. Critical Dynamic Stress. Figure 6 illustrates the evolution of accumulated strain as a function of vibration cycles. Apparently, the behavior can be categorized into stable, failure, and critical types. Table 5 provides the critical dynamic stress values for virgin expansive soil, 3% CSES, and 5% CSES.

Table 5 reveals that the critical dynamic stress range for 3% CSES falls between 21.6– and 34.9 kPa, whereas for 5%

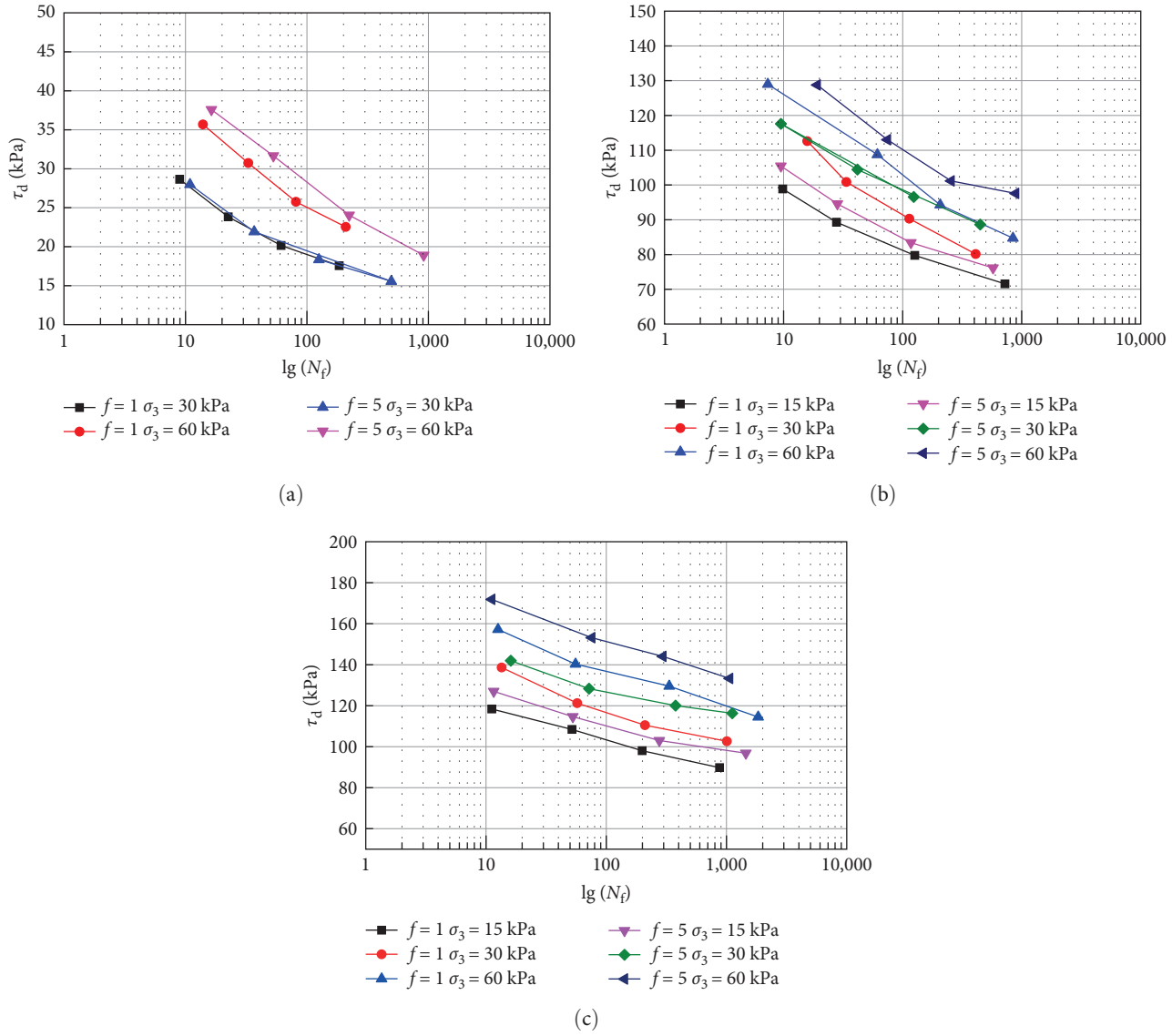

Figure 4: τ_f–lg (N_f) curves. (a) Virgin expansive soil. (b) Expansive soil improved with 3% cement content. (c) Expansive soil improved with 5% cement content.

Table 4: Dynamic shear parameters under different test conditions.

Frequency (Hz)	Virgin expansive soil		Expansive soil improved with 3% cement content		Expansive soil improved with 5% cement content	
	c_d (kPa)	φ_d (°)	c_d (kPa)	φ_d (°)	c_d (kPa)	φ_d (°)
1	10.5	15.4	24.1	38.3	32.6	31.2
5	12.3	8.4	25.2	36.2	36.5	22.4

CSES, it ranges from 145.6 to 249.7 kPa. When compared to the critical dynamic stresses of virgin expansive soil, the values for 3%–5% CSESs exhibit a significant increase of five to six times. Furthermore, when compared to the critical dynamic stresses of Group A filling, the mean critical dynamic stress of 3%–5% CSESs increases by 1.5–1.7 times. In contrast, the influence of frequency on critical dynamic stress is relatively weaker, while confining pressure exerts a more significant impact on critical dynamic stress.

The test data were amalgamated for regression analysis to delve deeper into the connection between confining pressure and critical dynamic stress, as illustrated in Figure 7.

As demonstrated in Figure 7, it can be inferred that critical dynamic stress exhibits a linearly increasing trend with

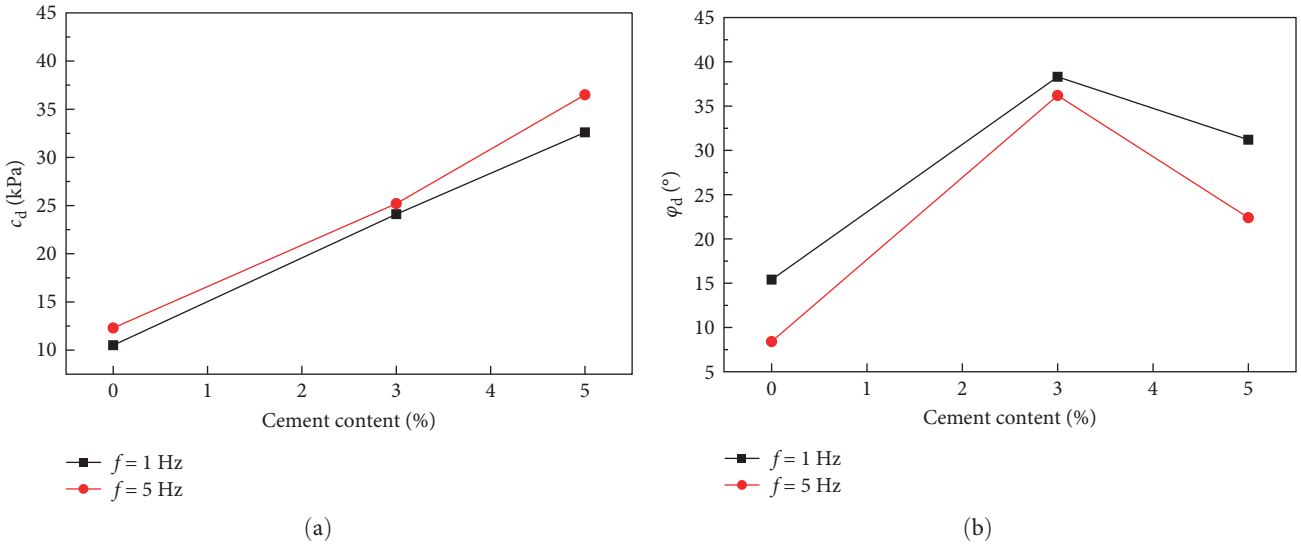

FIGURE 5: Change curve dynamic shear strength parameter. (a) Cohesion. (b) Friction angle..

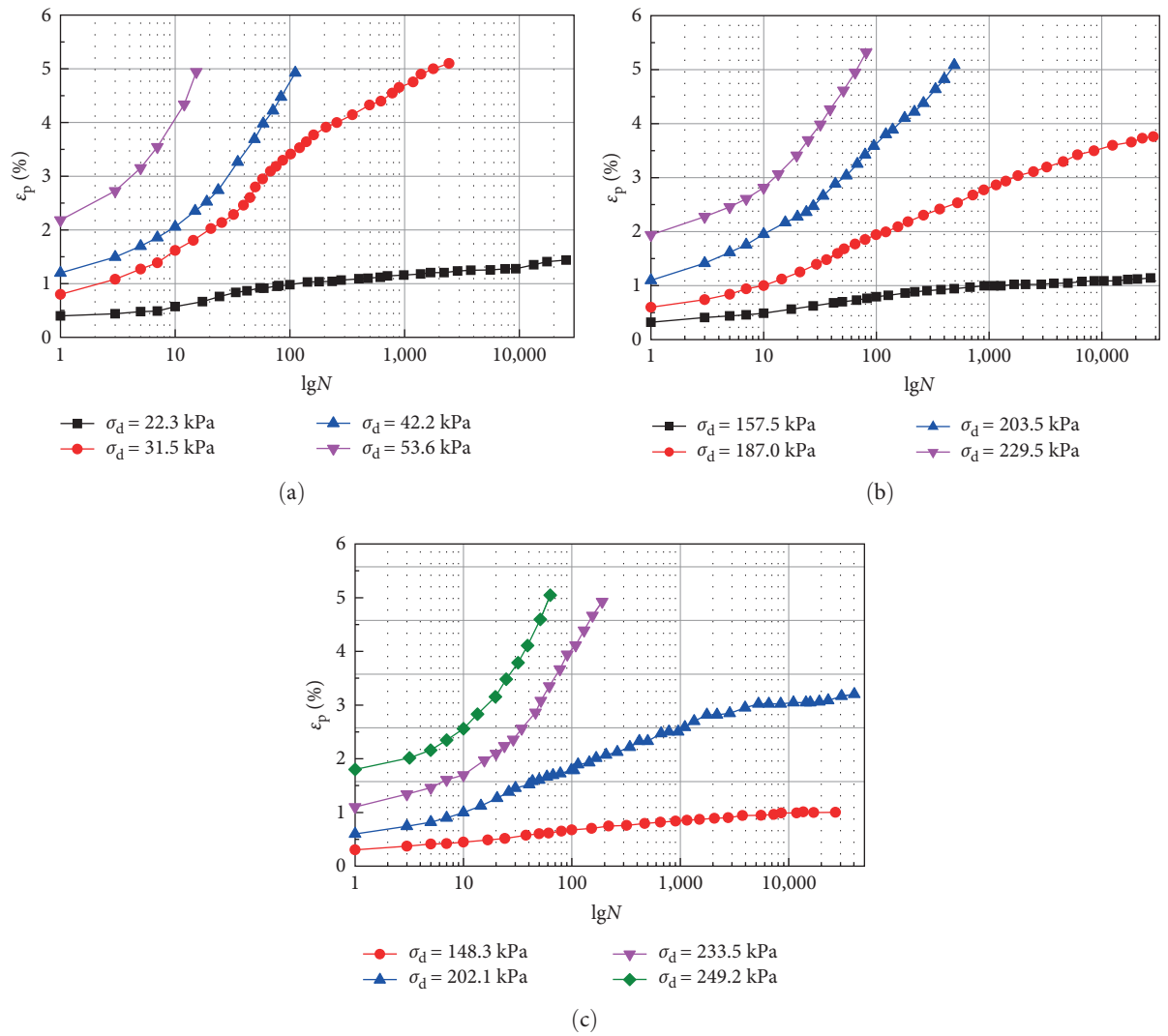

FIGURE 6: ε_p–lg$N$ curves (σ_d = 30 kPa, f = 1 Hz). (a) Virgin expansive soil. (b) Expansive soil improved with 3% cement content. (c) Expansive soil improved with 5% cement content.

Table 5: Critical dynamic stress.

Category	σ_d (kPa)	Frequency (Hz)	Critical dynamic stress (kPa)	Mean value (kPa)
Virgin expansive soil	30	1	22.3–31.5	26.90
	60	1	28.6–34.9	31.75
	30	5	21.6–30.8	26.20
	60	5	27.2–33.7	30.45
Expansive soil improved with 3% cement content	15	1	151.2–185.7	168.45
	30	1	157.5–203.5	180.50
	60	1	182.3–233.1	207.70
	15	5	148.8–181.4	165.10
	30	5	152.3–200.1	176.20
	60	5	180.6–229.6	205.10
Expansive soil improved with 5% cement content	15	1	142.5–208.1	175.30
	30	1	148.3–233.5	190.90
	60	1	202.5–249.7	226.10
	15	5	147.8–199.6	173.70
	30	5	145.6–231.7	188.65
	60	5	201.5–246.2	223.85
Group A filling	15	1	100.0–125.2	112.6
	30	1	100.1–125.2	112.7
	60	1	125.1–150.6	137.9

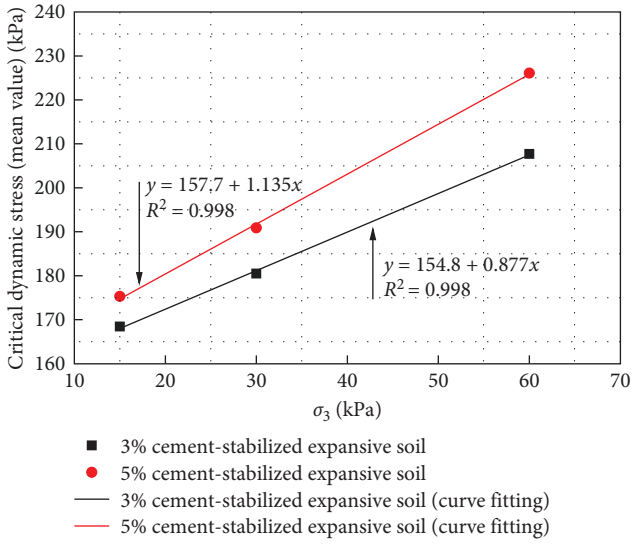

Figure 7: Critical dynamic stress under different confining pressure (1 Hz).

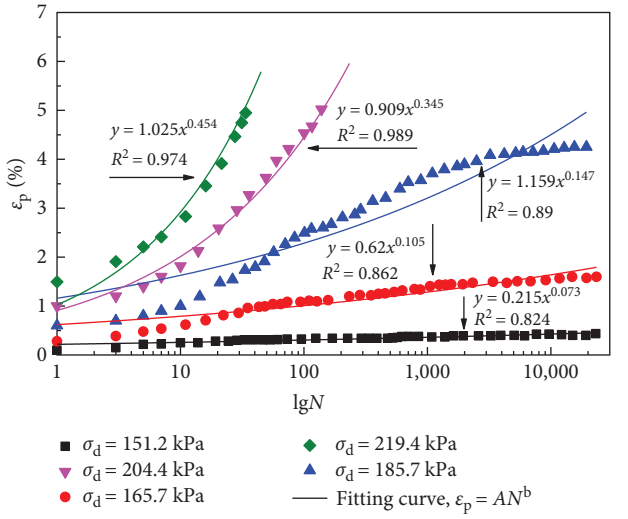

Figure 8: Fitting curves with Monismith model ($\sigma_3 = 15$ kPa, $f = 1$ Hz).

rising confining pressure, with correlation coefficients exceeding 0.998 in all cases. Given the relatively shallow burial depth of the subgrade bed, it experiences a decrease in critical dynamic stress attributable to the limited lateral confining pressure. Consequently, the subgrade bed bears the brunt of dynamic load effects, which can result in substantial accumulated deformation.

3.3. Cumulative Deformation. To explore an empirical model suitable for CSESs, the curve was first subjected to fitting and analysis using the Monismith model, taking CSES with a cement content of 3% as an example, as shown in Figure 8.

Figure 8 illustrates that the Monismith model provides a more effective fit for the failure curve, with correlation coefficients exceeding 0.974. However, for both the critical and failure curves, the correlation coefficient falls below 0.9 when using the Monismith model, resulting in a subpar fit. Regarding the stable curve, it is posited that its cumulative strain conforms to Equation (4):

$$\varepsilon_p = a + b \lg N, \tag{4}$$

where a and b are fitting parameters.

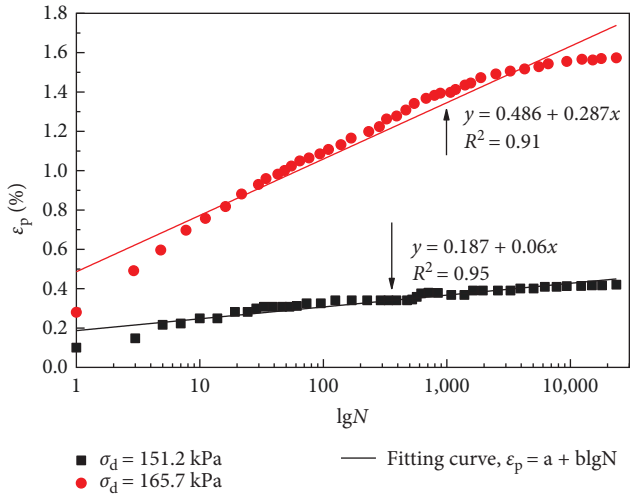

Figure 9: Fitting curves of $\varepsilon_p = a + b\lg N$ ($\sigma_3 = 15$ kPa, $f = 1$ Hz).

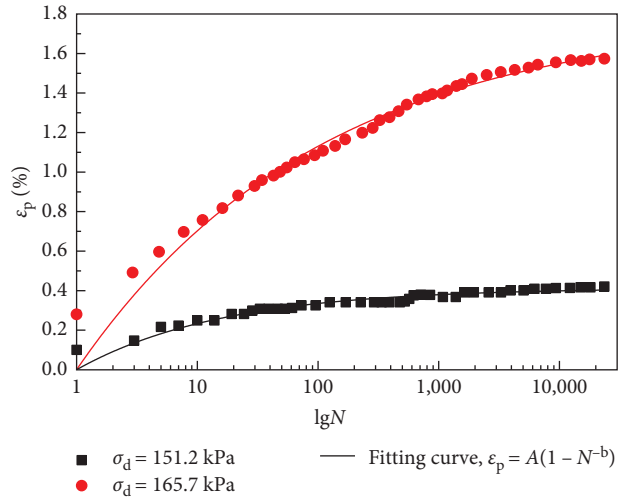

Figure 10: Fitting curves of Gidel model ($\sigma_3 = 15$ kPa, $f = 1$ Hz).

Table 6: Fitting parameters.

Test conditions	a	b
$f = 1$ Hz, $\sigma_3 = 15$ kPa, $\sigma_d = 151.2$ kPa	0.187	0.06
$f = 1$ Hz, $\sigma_3 = 15$ kPa, $\sigma_d = 165.7$ kPa	0.486	0.287
$f = 1$ Hz, $\sigma_3 = 30$ kPa, $\sigma_d = 157.5$ kPa	0.237	0.145
$f = 1$ Hz, $\sigma_3 = 60$ kPa, $\sigma_d = 182.3$ kPa	0.165	0.08
$f = 5$ Hz, $\sigma_3 = 15$ kPa, $\sigma_d = 150.3$ kPa	0.475	0.240

Table 7: A value under different test conditions.

Test conditions	A (%)
$f = 1$ Hz, $\sigma_3 = 15$ kPa, $\sigma_d = 151.2$ kPa	1.31
$f = 1$ Hz, $\sigma_3 = 15$ kPa, $\sigma_d = 165.7$ kPa	1.68
$f = 1$ Hz, $\sigma_3 = 30$ kPa, $\sigma_d = 157.5$ kPa	0.87
$f = 1$ Hz, $\sigma_3 = 60$ kPa, $\sigma_d = 182.3$ kPa	0.47
$f = 5$ Hz, $\sigma_3 = 15$ kPa, $\sigma_d = 150.3$ kPa	1.56

Equation (4) was employed to fit the stability curve, and the results are presented in Figure 9. It is evident from Figure 9 that the fitting performance for the stable curve surpasses that of the Monismith model. The fitting parameters for various test conditions are detailed in Table 6.

Table 6 illustrates that there is a considerable dispersion in the fitting parameters. This dispersion can be attributed to the factors influencing soil cumulative deformation, such as stress conditions, soil type, physical properties, and the vibration cycles. There are two parameters that encapsulate all influencing factors, and it is expected that these parameters will exhibit significant variations under different test conditions.

A permanent strain calculation model was introduced for subgrade soil subjected to cyclic loading, drawing upon extensive data from dynamic triaxial tests (see Equation (5)):

$$\varepsilon_p = A(1 - N^{-m}), \tag{5}$$

where ε_p is the cumulative strain under repeated load, A is the final cumulative strain, and m is the test parameter. The fitting results of the stability curve of CSESs by this method are shown in Figure 10.

Figure 10 illustrates that Equation (5) provides a superior fit for the stable curve compared to Equation (4). Consequently, according to Equation (5), this study proceeds to investigate an empirical model for cumulative deformation in CSES.

When $N \to +\infty$:

$$\varepsilon_{p,\max} = A. \tag{6}$$

That is, the coefficient A represents the cumulative maximum axial strain (see equation (6)), and the A value can be derived from the cumulative deformation curve under various test conditions, as presented in Table 7.

The cumulative strain coefficient α is calculated by normalizing the cumulative strain A value. By plotting the data points from various test conditions on the same graph, the relationship between α and N can be established, as illustrated in Figure 11.

Figure 11 reveals that the strain normalization values, even under various stress levels and physical states, tend to cluster within a remarkably narrow range. This clustering behavior can be effectively approximated using the following formula (refer to equation (7)):

$$\alpha = \varepsilon_p/\varepsilon_{p,\max} = 1 - N^{-b} \tag{7}$$

where $b = 0.277$.

Parameter A encapsulates the influence of soil stress state and amalgamates the value of A with the stress conditions.

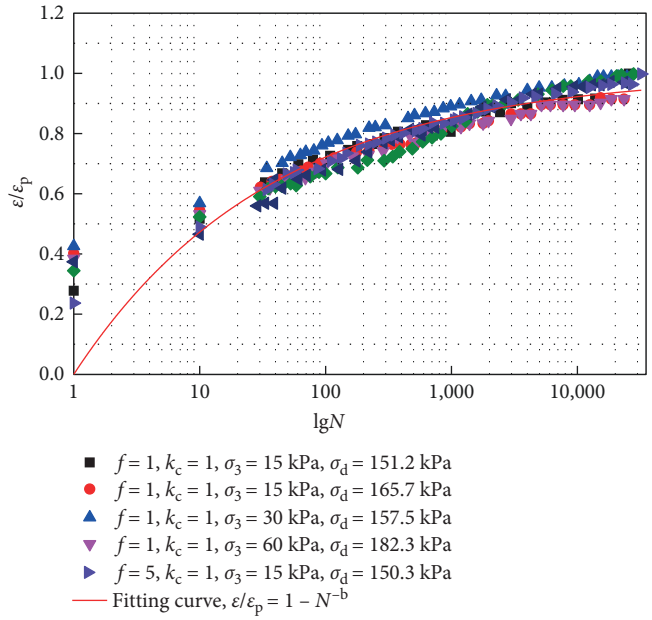

Figure 11: Relationship between α and lg$N$.

Table 8: Calculation parameters.

Test conditions	τ_d (kPa)	σ_3 (kPa)	σ_s (kPa)	σ_m (kPa)	SR_d	A (%)
$f = 1$ Hz, $\sigma_3 = 15$ kPa, $\sigma_d = 127.7$ kPa	63.85	15	0	7.5	8.51	1.31
$f = 1$ Hz, $\sigma_3 = 15$ kPa, $\sigma_d = 165.7$ kPa	82.85	15	0	7.5	11.05	1.68
$f = 1$ Hz, $\sigma_3 = 30$ kPa, $\sigma_d = 157.5$ kPa	78.75	30	0	15	5.25	0.87
$f = 1$ Hz, $\sigma_3 = 60$ kPa, $\sigma_d = 182.3$ kPa	91.15	60	0	30	3.04	0.47
$f = 5$ Hz, $\sigma_3 = 15$ kPa, $\sigma_d = 150.3$ kPa	75.15	15	0	7.5	10.02	1.56

Related findings indicate that the dynamic stress σ_d, confining pressure σ, and static deviatoric stress σ_s have great influence on the cumulative strain of soil. The dynamic shear stress ratio effectively synthesizes these three factors to comprehensively portray the stress state of the soil:

$$SR_d = \tau_d/\sigma_m, \tag{8}$$

where σ_m is the average stress, $\sigma_m = \sigma_3 + \sigma_s/2$, $\tau_d = \sigma_d/2$, and SR_d is the dynamic shear stress ratio. By incorporating Equation (8), the relationship between the dynamic shear stress ratio SR_d and the A value can be investigated. The calculation parameters are presented in Table 8 for reference.

Figure 12 illustrates a robust linear relationship between the dynamic shear stress ratio SR_d and the A value, with a correlation coefficient of 0.98. This relationship remains consistent across various test conditions. Consequently, the connection between the A value and the dynamic shear stress ratio SR_d can be expressed as $A = m + nSR_d$, where m and n represent the fitting parameters specific to the test.

Drawing from the aforementioned analysis, a cumulative deformation calculation model was proposed for the stability curve of CSESs:

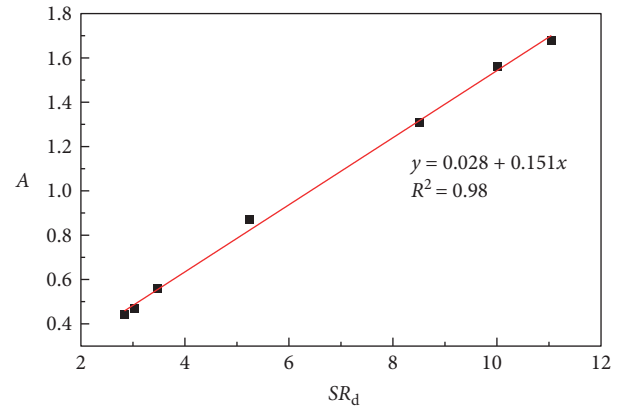

Figure 12: The correlation between the dynamic shear stress ratio SR_d and the A.

$$\varepsilon_p = (m + nSR_d)\left(1 - N^{-b}\right), \tag{9}$$

where m and n encompass the various factors that impact the stress state of the soil, contributing to cumulative strain. The parameter b reflects the relationship between the cumulative strain and the vibration cycles, obtained from the fitted

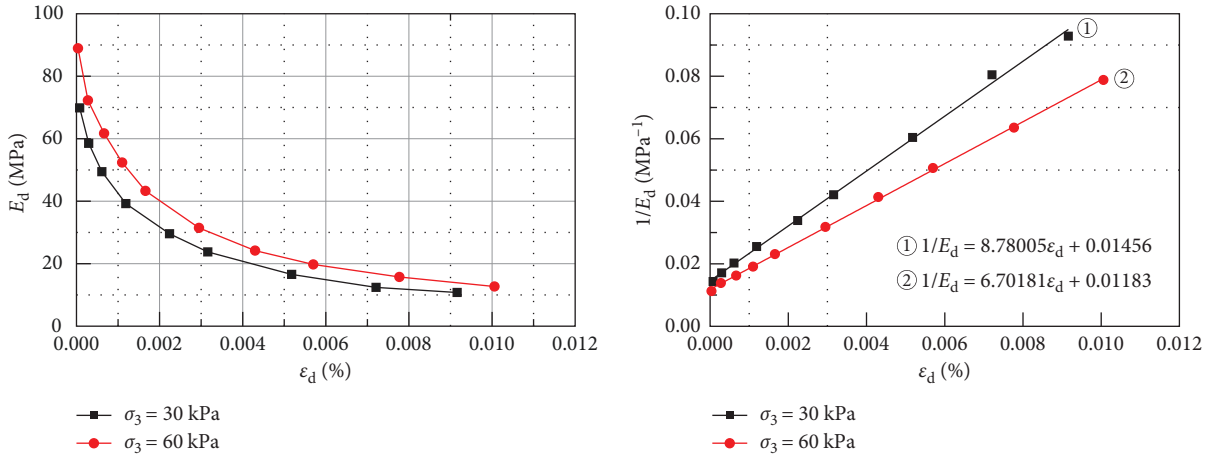

Figure 13: Virgin expansive soil (1 Hz). (a) E_d–ε_p curves and (b) $1/E_d$–ε_d curves.

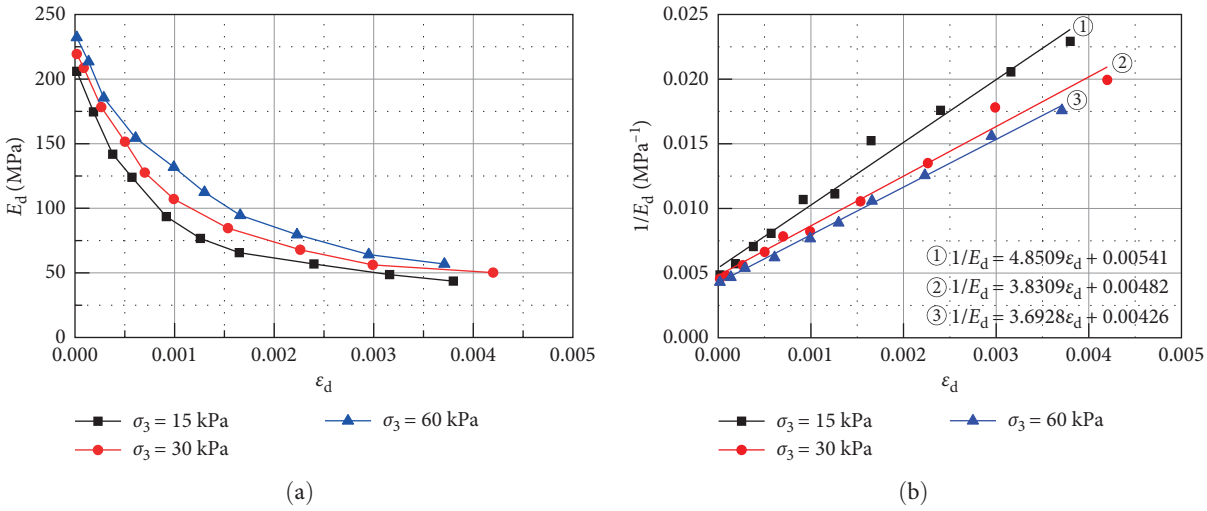

Figure 14: Expansive soil stabilized with 3% cement content (1 Hz). (a) E_d–ε_p curves. (b) $1/E_d$–ε_d curves.

relationship between the cumulative strain and N after normalization ($\varepsilon_p/\varepsilon_p$, max). The stress state emerges as the predominant factor influencing the parameters m and n, whereas soil type exerts the most substantial influence on parameter b.

3.4. Modulus of Elasticity and Damping Ratio. Figures 13–15 depict the E_d–ε_d and $1/E_d$–ε_d curve charts of virgin expansive soil and expansive soils improved with 3% and 5% cement content, respectively.

Figure 13 illustrates that within a small strain range of 0–0.002, the dynamic elastic modulus of virgin expansive soil experiences a notable decrease as strain increases, with the reduction reaching approximately 70%. Once the strain value exceeds 0.002, the dynamic elastic modulus stabilizes. This pattern is also observed in the case of 3% and 5% CSES, as depicted in Figures 14 and 15. The dynamic elasticity modulus of 3%–5% CSES exhibit an increase of approximately three to four times compared with that of virgin expansive soil. Due to the inherent difficulty of precisely measuring strain values within the 10^{-4} range in cyclic triaxial tests, E_d–ε_d curves cannot depict the variation pattern in the elastic stage, mainly manifested by a decline in the dynamic elastic modulus with increasing dynamic strain in the plastic deformation range. Furthermore, the regression analysis of the $1/E_d$–ε_d curves reveals that the correlation coefficients for both virgin expansive soil and CSES consistently surpass 0.97, thereby demonstrating a strong alignment between the test data and the fitted curves, with the minimal variability in the test data resulting in a high level of confidence in the results.

Figure 16 depicts the relationship between the damping ratio and strain for both virgin expansive soil and CSES. In the case of virgin expansive soil, the damping ratio exhibits a rapid increase within the strain range of 0–0.004, reaching up to 80% of its maximum value. Similarly, the damping ratio for CSES increases significantly within the strain range of 0–0.002, reaching approximately 70% of its maximum value. Table 9 presents the maximum dynamic elasticity moduli

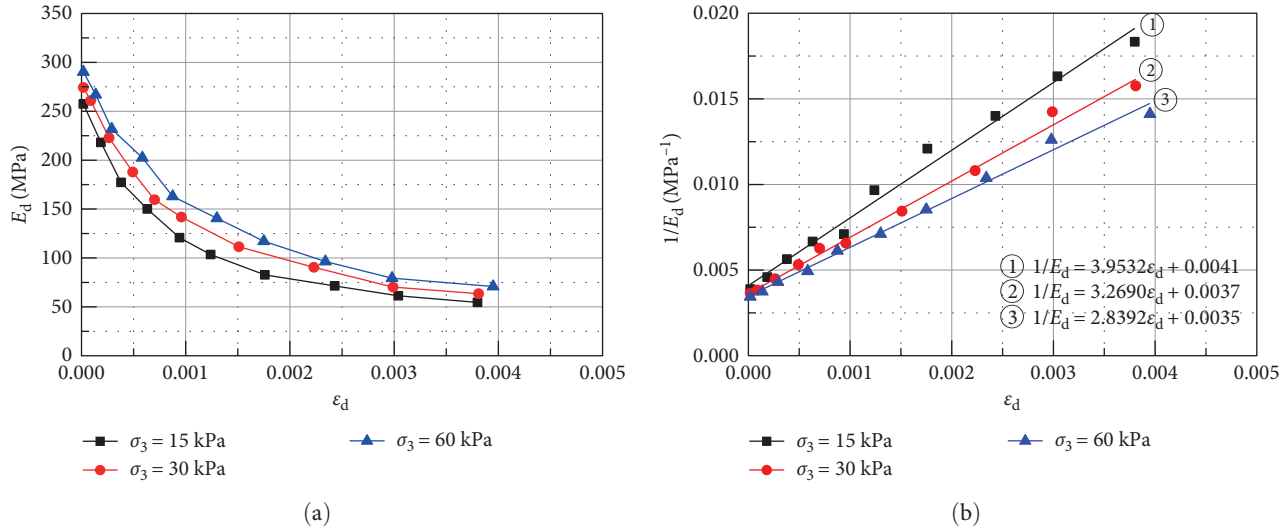

Figure 15: Expansive soil stabilized with 5% cement content (1 Hz). (a) E_d–ε_p curves. (b) $1/E_d$–ε_d curves.

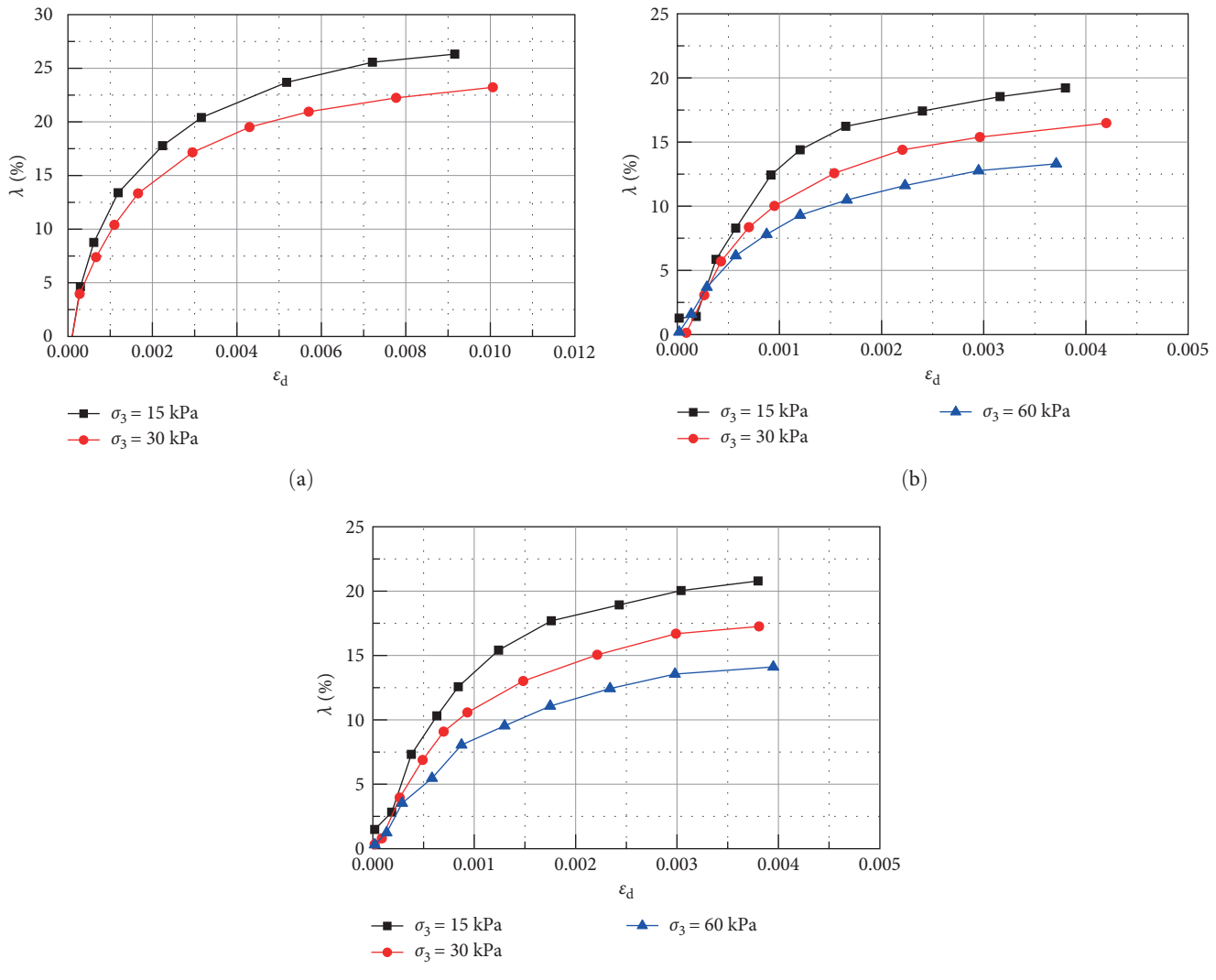

Figure 16: λ~ε_d curves (1 Hz). (a) Virgin expansive soil. (b) Expansive soil stabilized with 3% cement content. (c) Expansive soil stabilized with 5% cement content.

Table 9: Maximum dynamic elasticity moduli and maximum damping ratio.

f (Hz)	σ_3 (kPa)	Virgin expansive soil (MPa)		Expansive soil stabilized with 3% cement content (MPa)		Expansive soil stabilized with 5% cement content (MPa)	
		E_{dmax}	λ_{max}	E_{dmax}	λ_{max}	E_{dmax}	λ_{max}
1	15	68.68	31.21	184.84	25.16	243.90	26.77
	30	84.53	27.33	207.47	21.73	270.27	22.55
	60	—	—	234.74	17.56	285.71	18.76
5	15	79.11	38.21	215.05	29.14	270.27	28.15
	30	102.25	36.87	238.10	25.37	297.62	25.32
	60	—	—	242.72	19.33	322.58	17.59

and damping ratios for virgin expansive soil and expansive soils stabilized with 3% and 5% cement content. The maximum dynamic elasticity moduli range from 60 to 150 MPa for virgin expansive soil, 180–340 MPa for 3% CSES, and 240–350 MPa for 5% CSES. In contrast, the maximum damping ratios fall within the ranges of 18%–39% for virgin expansive soil, 11%–30% for 3% CSES, and 10%–29% for 5% CSES. These results indicate that the addition of cement significantly enhances the strength of expansive soil, while the change in damping ratio is relatively minor. The dynamic elasticity modulus exhibits an increasing trend with confining pressure, while the maximum damping ratio experiences a decrease with increasing confining pressure. Furthermore, both the maximum dynamic elasticity modulus and the maximum damping ratio show varying degrees of increase as the frequency is elevated.

A normalization analysis is conducted to further elucidate the correlation between the dynamic elastic modulus and the damping ratio of both virgin expansive soil and CSESs, as depicted in Figure 17.

Figure 17 illustrates that the relationship curve between E_d/E_{dmax} and ε_d largely falls within a narrow range, with minimal influence from the three factors of frequency, consolidation ratio, and confining pressure. This curve can be effectively fitted using the exponential function expressed in Equation (10):

$$\frac{E_d}{E_{d\,max}} = A + Be^{-C\varepsilon d}. \tag{10}$$

According to Equation (10), the following empirical formula for remodeling expansive soil can be obtained (see Equation (11)):

$$\frac{E_d}{E_{d\,max}} = A + Be^{-C\varepsilon d}. \tag{11}$$

Equation (11) can be transferred to:

$$\frac{E_d}{0.776e^{-474\varepsilon_d} + 0.188} = E_{dmax}. \tag{12}$$

The maximum dynamic modulus can be estimated using Equation (12). For instance, if E_d is 26.11 MPa and ε_d is 0.002, the maximum dynamic modulus can be calculated as 63.5 MPa, which is 5.18 MPa lower than the test value, resulting in a 7.5% error. These calculations indicate that the estimated value from the empirical fitting formula is slightly lower than the test value. Using the empirical fitting formula to estimate the dynamic modulus can be considered as providing a certain safety margin.

In a similar manner, employing Equation (10), the following empirical formula for 3% and 5% CSESs can be derived:

$$\frac{E_d}{0.778e^{-857\varepsilon_d} + 0.221} = E_{dmax} \tag{13}$$

$$\frac{E_d}{0.739e^{-1163\varepsilon_d} + 0.211} = E_{dmax} \tag{14}$$

$$\lambda = \lambda_{max}\left(1 - \frac{E_d}{E_{d\,max}}\right). \tag{15}$$

By incorporating Equations (12)–(14) into Equation (15), an empirical formula for estimating the full strain λ can be obtained. Among these, Equations (16)–(18), respectively, correspond to virgin expansive soil, expansive soil improved with 3% cement content, and expansive soil improved with 3% cement content.

$$\lambda = \lambda_{max}(0.812 - 0.776e^{-474\varepsilon_d}) \tag{16}$$

$$\lambda = \lambda_{max}(0.779 - 0.778e^{-857\varepsilon_d}) \tag{17}$$

$$\lambda = \lambda_{max}(0.789 - 0.739e^{-1163\varepsilon_d}), \tag{18}$$

where ε_d is the dynamic strain and λ_{max} is the asymptotic constant when $\varepsilon_d > 10^{-3}$ in the test, which is determined by the test.

Additionally, it is noticeable from equations (12)–(14) that there is a residual modulus of 0.188, 0.221, and 0.211

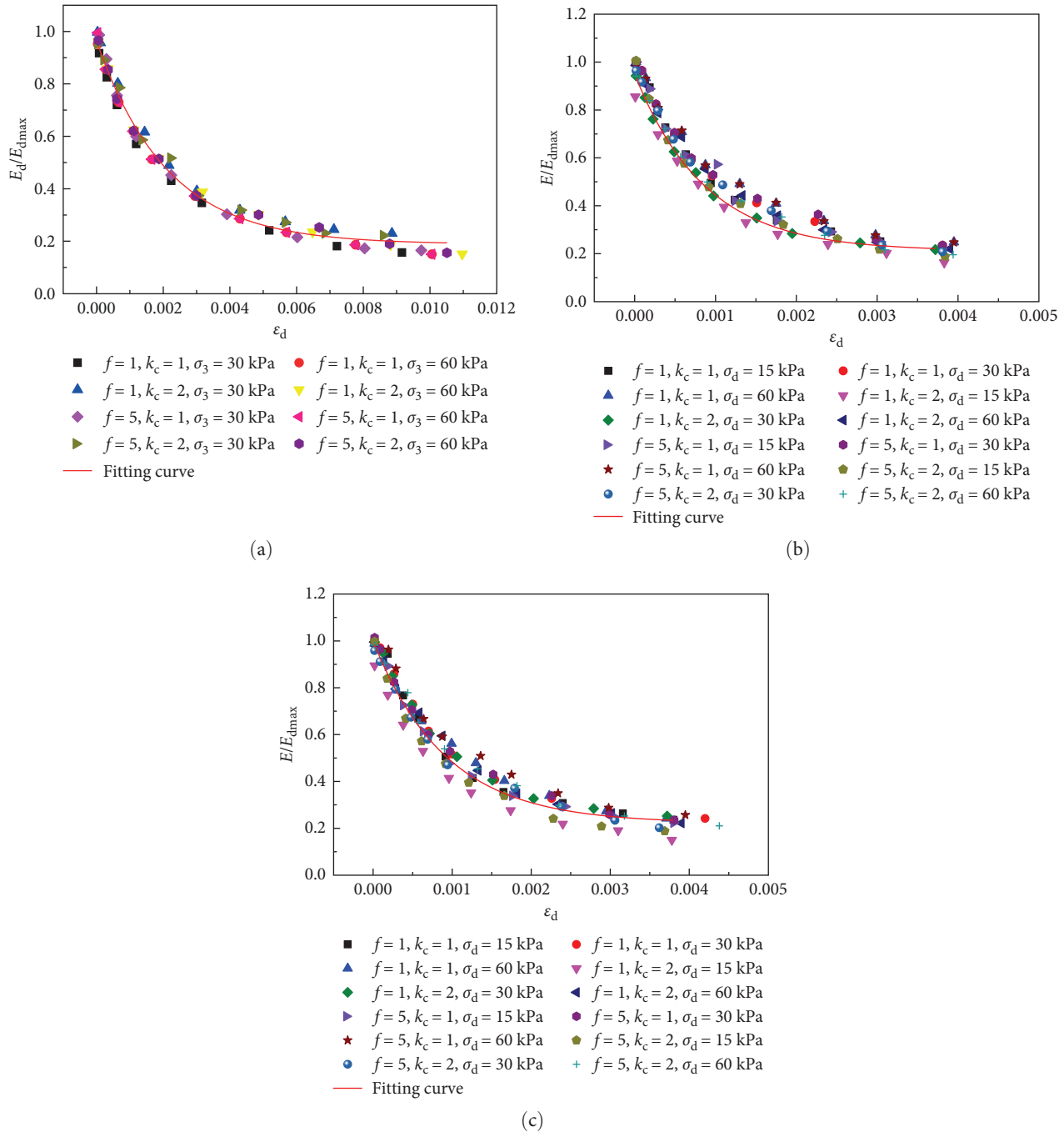

FIGURE 17: E_d/E_{dmax}–ε_d fitting curve. (a) Virgin expansive soil. (b) Expansive soil stabilized with 3% cement content. (c) Expansive soil stabilized with 5% cement content.

for virgin expansive soil, expansive soil improved with 3% cement content, and expansive soil improved with 3% cement content, respectively. This residual modulus does not tend to zero with the increase of dynamic strain, which is not representative of practical conditions. This situation arises because dynamic triaxial tests can only analyze the dynamic stress–strain relationship within the range of 10^{-4}–10^{-2} strain. Beyond this range, the soil still exhibits a certain residual modulus in the dynamic behavior. Hence, caution should be exercised when applying these empirical formulas.

3.5. Measured Dynamic Stress Level of the Subgrade. Figure 18 depicts the dynamic stress variation with respect to the subgrade depth under various loading conditions during the excitation test, specifically under dry subgrade conditions.

As illustrated in Figure 18, the dynamic stress variation and attenuation pattern along the subgrade depth align with the test acceleration. At different train speeds, specifically 120, 140, 160, 180, and 200 km/hr, with an axle load of 21 tons, the dynamic stress at the subgrade surface measures 83.02, 89.13, 92.61, 96.13, and 103.02 kPa, respectively. The

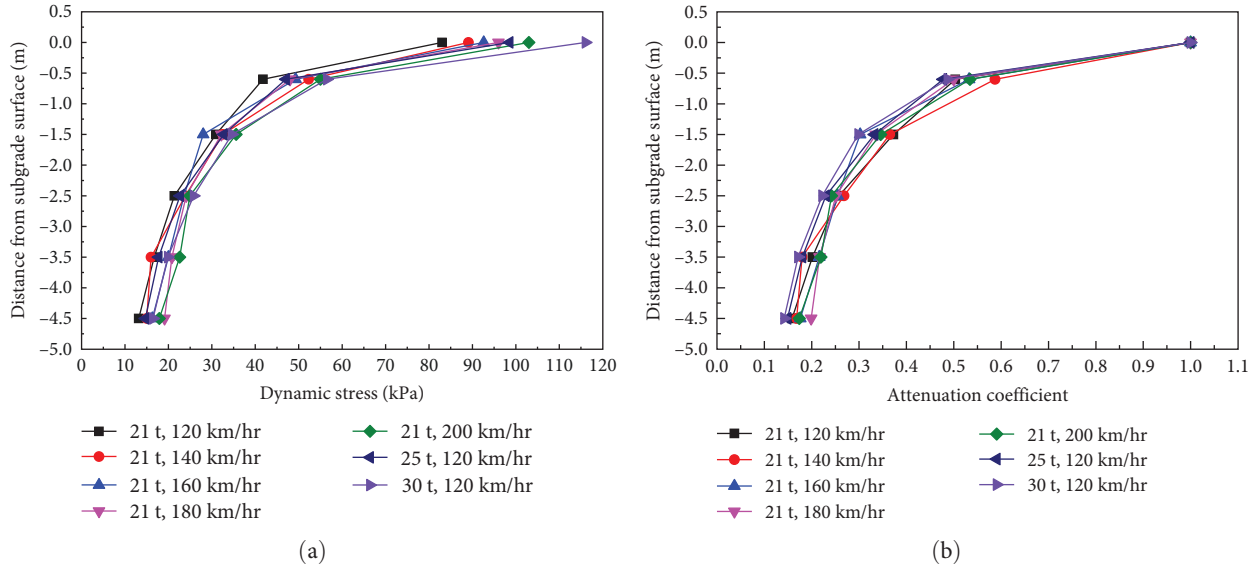

FIGURE 18: Change curve of dynamic stress along the subgrade depth. (a) Change curve and (b) attenuation curve.

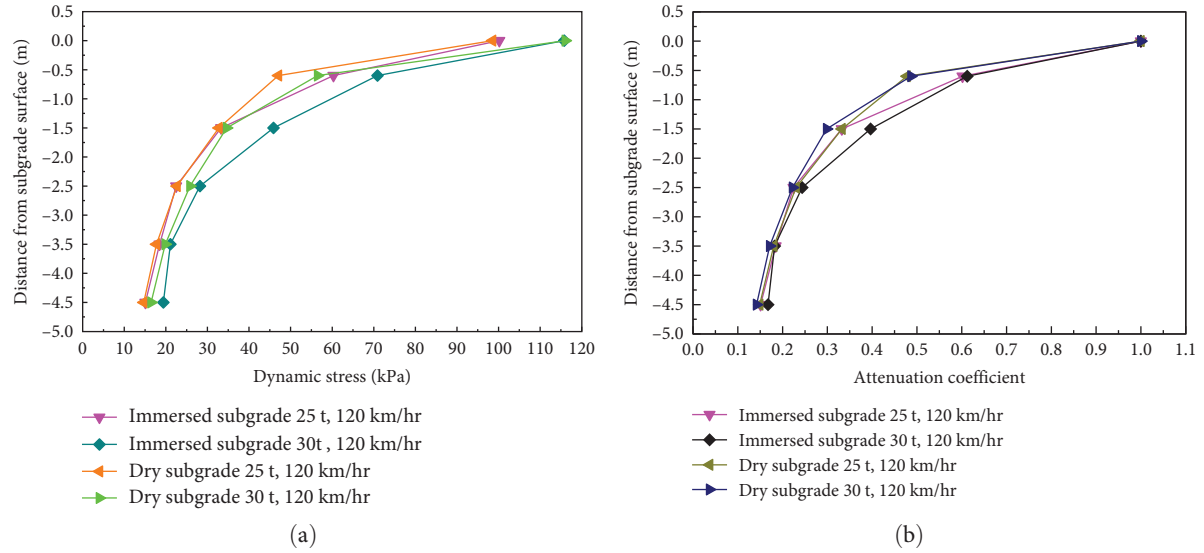

FIGURE 19: Comparison curve of dynamic stress along the subgrade depth. (a) Change curve. (b) Attenuation curve.

dynamic stress at the subgrade surface registers 98.57 and 116.07 kPa when the train speed is 120 km/hr, with axle loads of 25 and 30 tons, respectively. It is noteworthy that the overall consistency of the attenuation curve for dynamic stress along the subgrade depth is superior to that of the acceleration curve. The dynamic stress experiences a maximum attenuation of 40% and 80% on the surface and bottom layers of the subgrade bed, respectively. Furthermore, the maximum dynamic stress at the subgrade surface constitutes approximately 58.03% of the measurement range of the testing element, ensuring the element's continuous and effective operation.

Figure 19 presents the comparative dynamic stress curve of the subgrade under dry and submerged conditions. It is evident that the dynamic stress amplitude at the subgrade surface remains consistent under identical test conditions, whether in a dry or submerged state. This observation suggests that the load transmitted from the upper excitation system to the subgrade surface remains unchanged. In the context of subgrade soaking, the dynamic stress within the subgrade bed exhibits a "rise–fall" pattern along the depth of the subgrade, with the most significant difference occurring at a depth of approximately 1.5 m beneath the subgrade surface. The maximum dynamic stress under submerged conditions is approximately 1.02–1.28 times than that observed in the dry condition. This disparity can be attributed to the increase in subgrade moisture content during immersion, leading to elevated pore water pressure and reduced effective

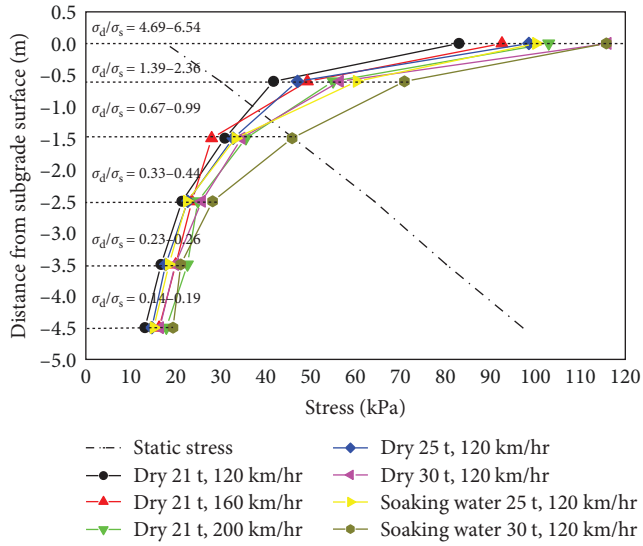

Figure 20: Curves of dynamic and static stress along the subgrade depth.

Table 10: Comparison between the dynamic stress amplitude of the subgrade and the critical dynamic stress.

Subgrade depth (m)	Dynamic stress level of the subgrade (kPa)		Critical dynamic stress (kPa)	Evaluation result
	25 tons, 120 km/hr	30 tons, 120 km/hr		
0–0.6	60.3–100.2	70.9–115.8	257–380	Meet stability
0.6–2.5	22.5–60.3	28.2–70.9	148.8–233.1	Meet stability
2.5–4.5	15.1–22.5	19.4–28.2	142.5–249.7	Meet stability

stress. Consequently, the dynamic stress threshold for failure is lowered.

In summary, the distribution patterns and attenuation coefficients of dynamic stress along the subgrade depth remain consistent under both immersion and drying conditions. This observation suggests that the CSES subgrade exhibits excellent compaction, sealing, and high construction quality, rendering it less susceptible to environmental effects such as rainfall during its service life. Additionally, the railway subgrade design incorporates a comprehensive drainage system, resulting in most rainwater being efficiently diverted as surface runoff. Consequently, the infiltration of water into the subgrade bed is relatively minimal and significantly weaker compared to the conditions observed in this test. Hence, whether the subgrade is in a dry or immersed state, the dynamic stress difference experienced by the CSES subgrade in heavy-haul railway operation remains relatively minimal, with a correspondingly modest increase in severity. However, it is important to note that this assessment does not account for issues related to deep infiltration resulting from the degradation of subgrade fillings.

3.6. Dynamic Stability Assessment of Subgrade. Dynamic stress, resulting from the vibration load on the upper part of the subgrade, distributes both horizontally and vertically, with a particular focus on the depth of vertical influence [12]. In this study, the vertical depth of dynamic stress distribution is examined using the dynamic-to-static stress ratio ($\sigma_d/\sigma_s > 0.2$), as depicted in Figure 20 [14–16].

Figure 20 illustrates the gradual reduction of dynamic stress with increasing subgrade depth, while concurrently, static stress exhibits a gradual increase with greater depth within the subgrade. The calculated dynamic and static stress ratio at a subgrade depth of 2.5 m ranges from 0.33 to 0.44, surpassing the threshold of 0.2. This suggests that the dynamic influence depth extends beyond the 2.5 m subgrade thickness. The dynamic and static stress ratios at subgrade depths of 3.5 and 4.5 m are observed to be 0.23–0.26 and 0.14–0.19, respectively. These values suggest that the dynamic influence depth of the subgrade, under the dynamic load of heavy-duty trains, ranges from 3.5 to 4.5 m. Given that the depth of dynamic influence surpasses the designated subgrade bed thickness, it is imperative to validate the dynamic stability of the subgrade structure.

Table 10 presents a comparison between the dynamic stress levels within the subgrade and the critical dynamic stress of the filler. It is worth noting that the dynamic stress values listed in Table 10 pertain to subgrade testing conducted under immersion conditions, with slight variations observed in the dynamic stress levels when compared to dry conditions.

Table 10 demonstrates that within the dynamic influence depth range, the dynamic stress levels in the subgrade remain below the critical dynamic stress of the filler at the corresponding

position. This observation signifies that the dynamic stability of 3%–5% CSES, utilized as subgrade fill material for heavy-haul railways, adheres to the requisite criteria.

4. Conclusion

In this investigation, relying on Haoji (Haolebaoji-Ji'an, China) heavy-haul railway engineering, cyclic triaxial tests were executed to scrutinize the dynamic attributes exhibited by the CSESs across a series of diverse cyclic stress, confining pressures, and frequencies. Concurrently, in situ vibration trials were undertaken to dissect the dynamic characteristics inherent to the CSES subgrade. This investigation can provide a feasibility reference for the design of heavy-haul railways. The main conclusions are as follows:

(1) Upon incorporating cement into the expansive soil, a noteworthy enhancement in both strength and water stability is observed, coupled with a remarkable improvement in the expansion and contraction properties, affirming the soundness of the improvement approach. In contrast to lime modification, the use of cement under equivalent dosage conditions yields higher strength in CSES.

(2) Critical dynamic stress exhibits a strong linear correlation with confining pressure. In equivalent conditions, the critical dynamic stress of 3%–5% CSES surged by a notable five- to sixfold when compared to virgin expansive soil. Furthermore, on average, it reached approximately 1.5–1.7 times than that of Group A filler.

(3) The dynamic elastic modulus of CSES exhibits a declining trend as the strain level increases, accompanied by a corresponding rise in the damping ratio, with the most significant reduction and subsequent increase occurring within a narrow strain range. Additionally, the maximum dynamic elastic modulus progressively increases with higher levels of confining pressure and frequency.

(4) An empirical formula has been developed to estimate both the maximum dynamic modulus and damping ratio of CSES. Furthermore, an empirical formula has been formulated to predict the cumulative deformation of cement-improved expansive soil, which takes into account factors such as the vibration cycles and stress amplitude.

(5) In the in situ vibration test, the dynamic stress at the subgrade surface ranges from 98.57 to 116.07 kPa for heavy-haul trains, which is higher than the range of 83.02–103.02 kPa for passenger trains. When the subgrade is immersed in water, the dynamic stress increases by a factor of 1.02–1.28 compared to the dry state of the subgrade. Furthermore, the depth of dynamic stress influence extends to 3.5–4.0 m, surpassing the designed thickness of the subgrade bed (2.5 m).

(6) The utilization of CSES as subgrade filling for heavy-haul railways leads to a significant increase in the critical dynamic stress at the same location compared to that observed during in situ vibration tests. This observation confirms that employing CSES as subgrade filling for heavy-haul railways meets the operational performance requirements under prolonged train load conditions.

Data Availability

Data will be made available on request.

Conflicts of Interest

The authors declare that they have no conflicts of interests.

Authors' Contributions

Yonghui Shang is responsible for conceptualization, methodology, supervision, and funding acquisition. Linrong Xu is responsible for software, experiment, data curation, visualization, writing-original draft, and writing-review and editing. Xiaofei Hao is responsible for supervision and funding acquisition. Qichuan Zhu is responsible for writing-original draft and writing—review and editing. Donghong Li is responsible for writing—review and editing.

Acknowledgments

This work is financially supported by the National Natural Science Foundation of China (grants no. 42172322, no. U2268213, and no. 42007419), the Key Research and Development Project of the Department of Science and Technology in Henan Province of China (grants no. 232102241040; no. 202102310264), and the Huanghuai University Cultivation Fund Project (grant no. XKPY-2022017).

References

[1] H. Gadouri, "Behavior of natural pozzolana-lime-stabilized clayey soils artificially contaminated by sulfates," *Jordan Journal of Civil Engineering*, vol. 17, no. 4, 2023.

[2] H. Gadouri and B. Mezian, "Strength improvement using polypropylene fiber as reinforcement in natural pozzolana-lime-stabilized expansive clayey soil artificially contaminated by sulfates," *Periodica Polytechnica Civil Engineering*, vol. 67, no. 4, pp. 1152–1175, 2020.

[3] H. Gadouri, K. Harichane, and M. Ghrici, "Effect of calcium sulphate on the geotechnical properties of stabilized clayey soils," *Periodica Polytechnica Civil Engineering*, vol. 61, no. 2, pp. 256–271, 2017.

[4] H. Gadouri, K. Harichane, and M. Ghrici, "Effect of sodium sulphate on the shear strength of clayey soils stabilised with additives," *Arabian Journal of Geosciences*, vol. 10, no. 10, Article ID 218, 2017.

[5] W. Zhai, C. Cai, and K. Wang, "Experimental study on fatigue performance and cumulative damage of bottom structure of heavy-duty railway tunnel," *China Railway Science*, vol. 40, no. 4, pp. 77–85, 2019.

[6] A. T. Daloglu and C. G. Vallabhan, "Values of k for slab on winkler foundation," *Journal of Geotechnical and Geoenvironmental Engineering*, vol. 126, no. 5, pp. 463–471, 2000.

[7] L. Frýba, "History of winkler foundation," *Vehicle System Dynamic*, vol. 24, no. sup1, pp. 7–12, 1995.
[8] V. V. Krylov, "Generation of ground vibrations by superfast trains," *Applied Acoustics*, vol. 44, no. 2, pp. 149–164, 1995.
[9] W. Zhai, C. Cai, and K. Wang, "Dynamics assessment method for design of high speed railway plan and profile," *High Speed Railway Technology*, vol. 1, no. 1, pp. 1–5, 2010.
[10] Y. M. Chen and X. C. Bian, "The review of high-speed railway track foundation dynamics," *China Civil Engineering Journal*, vol. 51, no. 6, pp. 1–13, 2018.
[11] L. Wuming, N. Rusong, and L. Wenjie, "Random distribution characteristics of peak dynamic stress on subgrade surface of heavy haul railway," *Rock and Soil Mechanics*, vol. 40, no. 4, pp. 1603–1613, 2019.
[12] W. Q. Lv, Q. Luo, and G. Liu, "Structural analysis and design method for subgrade bed of heavy haul railway," *Journal of the China Railway Society*, vol. 38, no. 4, pp. 74–80, 2016.
[13] W. Leng, H. Mei, R. Nie, W. Liu, Y. Su, and S. Tang, "Full-scale model test of heavy haul railway subgrade," *Journal of Vibration and Shock*, vol. 37, pp. 1–6, 2018.
[14] L.-L. Wang, G.-L. Yang, Y.-H. Fang, P.-F. Wang, and Y.-B. Xu, "In-situ tests on dynamic character of fully-enclosed cutting subgrade of high-speed railways in expansive soil areas," *Chinese Journal of Geotechnical Engineering*, vol. 36, no. 4, pp. 640–645, 2014.
[15] D. Li, Q. Su, T. Liu, K. Xie, and Y. Guo, "Experimental study on dynamic characteristics of ballastless track in pile-plank structure subgrade-bridge transition section," *Railway Standard Design*, vol. 63, no. 10, pp. 56–60, 2019.
[16] Y. Shang, L. Xu, Y. Xu, and Y. Li, "Field test study on a short pile-net composite foundation over gravel clay for high-speed railways," *Journal of Engineering Science and Technology Review*, vol. 9, no. 3, 2016.
[17] B. O. Hardin and W. L. Black, "Vibration modulus of normally consolidated clay," *Journal of the Soil Mechanics and Foundations Division*, vol. 94, no. 2, pp. 353–369, 1968.
[18] H. B. Seed, "Soil moduli and damping factors for dynamic response analyses," Reoprt, EERC 70-10, 1970.
[19] P. Wang, H. Xu, and R. Chen, "Effect of cement asphalt mortar debonding on dynamic properties of CRTS II slab ballastless track," *Advances in Materials Science and Engineering*, vol. 2014, Article ID 193128, 8 pages, 2014.
[20] H. B. Seed, P. P. Martin, and J. Lysmer, "Pore-water pressure changes during soil liquefaction," *Journal of the Geotechnical Engineering Division*, vol. 102, no. 4, pp. 323–346, 1976.
[21] Q. F. Xie, G. B. Liu, and S. T. Fan, "A study of dynamic characteristics of the saturated remolded clayey silt under circle load," *Hydrogeology & Engineering Geology*, vol. 1, pp. 78–83, 2017.
[22] G. L. Yang, M. M. Qiu, X. He, and Q. Shen, "Tests for working property of water-proof layer of cutting subgrade in expansive soil under vibrating load," *Journal of Vibrattion and Shock*, vol. 35, no. 5, pp. 1–7, 2016.